

Scaling of graphene field-effect transistors supported on hexagonal boron nitride: radio-frequency stability as a limiting factor

Pedro C. Feijoo^{,a}, Francisco Pasadas^a, José M. Iglesias^b, María J. Martín^b, Raúl Rengel^b, Changfeng Li^c, Wonjae Kim^{c,d}, Juha Riihonen^c, Harri Lipsanen^c, David Jiménez^a*

^a Departament d'Enginyeria Electrònica, Escola d'Enginyeria, Universitat Autònoma de Barcelona, 08193 Bellaterra, Spain

^b Departamento de Física Aplicada, Universidad de Salamanca, Salamanca 37008, Spain

^c Department of Electronics and Nanoengineering, Aalto University, 02150 Espoo, Finland

^d VTT Technical Research Center of Finland, 02150 Espoo, Finland

** Corresponding author: PedroCarlos.Feijoo@uab.cat*

Keywords

graphene, boron nitride, carrier mobility, scattering mechanisms, radio-frequency, short channel, small-signal

Electronic supplementary information (ESI) available.

Abstract

Graphene has hugely increased its quality in nanodevices thanks to hexagonal boron nitride (hBN) acting as a supporting layer. Here, we investigate to which extent hBN and channel length scaling can be exploited in graphene field-effect transistors (GFETs) to get competitive radio-frequency (RF) performances. For such a purpose, we have applied multi-scale physics-based techniques to assess the scalability of the transistor RF performance via reduction of the channel length. To capture the specific physics of graphene supported on hBN, the carrier density dependent mobility and saturation velocity were obtained from an

ensemble Monte Carlo simulator that deals with the relevant scattering mechanisms, such as intrinsic phonons, scattering with impurities and defects, surface polar phonons with the substrate and gate dielectric, and electron-electron interactions. This information is fed into a self-consistent simulator, which solves the drift-diffusion equation coupled with the two-dimensional Poisson's equation to take full account of short channel effects. The GFET electrical characteristics obtained with the simulator were benchmarked against experimental data from our fabricated devices. RF performance and stability were evaluated as a function of the channel length from a charge-conserving small-signal model. We found that device instability poses a hard limit on the expected benefit that scalability is supposed to bring in terms of RF performance. A careful choice of the bias point is necessary to avoid instability, although at the expense of getting smaller performance. Despite this, maximum oscillation frequencies in the THz region are still achievable for channel lengths of few hundreds of nanometers.

1. Introduction

Graphene promises to stand out as a channel material in analog radio-frequency (RF) electronics due to its two-dimensional character and carrier transport properties: a mobility up to $2 \cdot 10^5 \text{ cm}^2 \text{ V}^{-1} \text{ s}^{-1}$ and a high saturation velocity of $4 \cdot 10^7 \text{ cm s}^{-1}$.¹⁻⁵ Besides, graphene presents a remarkably high mechanical strength, with an elastic modulus of up to 550 N m^{-1} and a breaking strength of up to 35 N m^{-1} ,^{6,7} which also makes it a feasible channel material for flexible electronics. Nevertheless, the transport properties decrease significantly when graphene is the active part of a substrate supported device because of the charge scattering.^{1,8} Hexagonal boron nitride (hBN), however, with an atomically perfect surface relatively free of dangling bonds and charge traps, has proved to be an exceptional dielectric for graphene field-effect transistors (GFETs).⁹ Graphene devices fabricated on hBN exhibit up to one order-of-magnitude improvement in mobility and carrier inhomogeneities in comparison with conventional oxide dielectrics.¹⁰

In the effort to successfully develop the next-generation of GFET supported on hBN technology, device simulation tools must describe accurately both the electrostatics and carrier transport across the graphene taking into account the specificity of the graphene/hBN interaction. An appropriate description of the carrier transport requires the inclusion of the relevant scattering mechanisms that drive the carrier mobility and saturation velocity. In a previous work¹¹ we developed a self-consistent model that solved the drift-diffusion transport equation coupled with the two-dimensional (2D) Poisson's equation in order to study the short channel effects in GFETs. However, both mobility and saturation velocity were considered constant, so the model ignored the complexity of the interplay among the scattering processes that, in fact, strongly depend on carrier density. In this paper, we have

considered the various scattering mechanisms, including the specific influence of the hBN substrate on the carrier transport. For this purpose, carrier transport properties were calculated by a self-consistent ensemble Monte Carlo (EMC) simulator for graphene that allows to assess the role played by each type of scattering.^{12,13} This information is fed into the self-consistent GFET model to obtain current-voltage (I-V) characteristics. Additionally, we have formulated a small-signal model of the GFET composed by parameters extracted from linearization around a bias point of direct current (DC) simulations. Different from what the studies ever reported so far, the proposed model guarantees charge conservation, which is essential for accurate calculations of the transistor RF figures of merit (FoM). These kind of models are required to bridge the gap between both device and circuit levels and to make comparisons with other existing RF technologies, e.g. those based on Si or III-V compounds.¹⁴ Importantly, our GFET simulator and corresponding small-signal model can deal with short-channel effects (SCE), which significantly reduce the expected cutoff (f_T) and maximum oscillation (f_{max}) frequencies¹¹ with respect to the simple projection derived from the long-channel behavior. Also, we have investigated the stability of a GFET when it operates as an amplifier using the small-signal model combined with microwave-engineering techniques. We specifically look into the dependence of stability on both channel length and graphene quality. Lack of stability can prevent a transistor from working as an amplifier within the targeted RF window, so it is desirable to know the conditions that ensure stability and to estimate the possible trade-off with the power gain.

First, this article briefly describes the drift-diffusion based simulator. Then, we discuss the methodology used to extract the mobility and saturation velocity taking full account of the intrinsic scattering mechanisms, the presence of impurities and defects across the graphene

sheet, and the interactions with the substrate and top gate dielectric. Next, the small-signal model is presented, emphasizing the relevance of guaranteeing charge conservation. The simulator has been benchmarked against DC experimental results from our fabricated devices. Using this model we have investigated the scalability of GFETs supported on hBN targeting RF applications. This has been carried out with assumption of different scenarios for both impurities and defects concentrations. The final part of this work thoroughly studies the RF stability of GFETs.

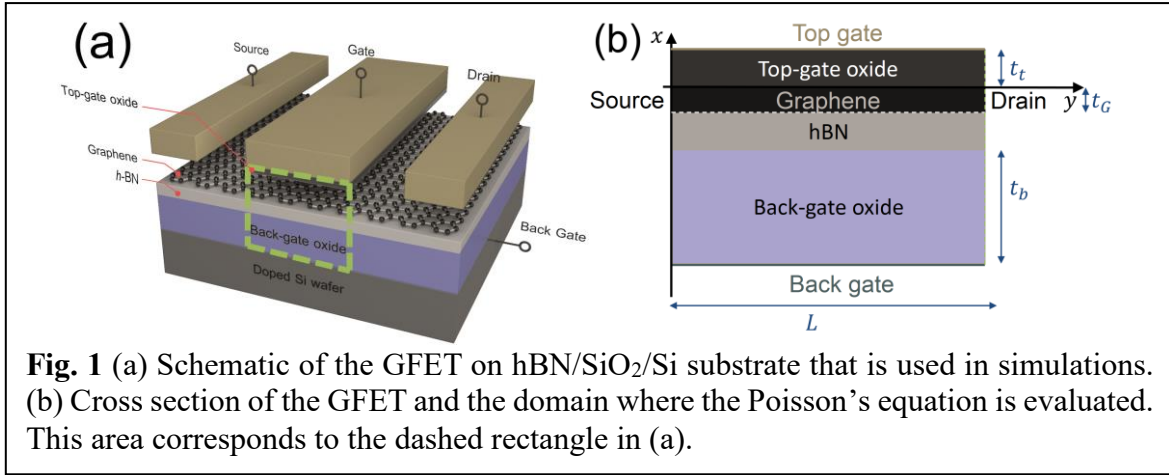
2. Methods

2.1 Self-consistent simulator

The dual-gate GFET studied here is represented in Fig. 1a and is based on a structure where a graphene layer is encapsulated between thin layers of hBN and Al₂O₃. The hBN, with a thickness of the order of tens of nanometers, acts as the supporting intermediate layer on the substrate while the Al₂O₃ layer plays the role of the top gate insulator. The n-type Si substrate is also utilized as a back gate electrode. We have neglected the influence of the thin hBN layer in the electrostatics calculations since its contribution to the back gate capacitance is relatively small. However, we do have considered its influence on the electronic transport through the calculation of low-field mobility μ_{LF} and velocity saturation v_{sat} . Regarding the electronic transport, the drift-diffusion mechanism was considered as an appropriate description, although this assumption can only be applied if the mean free path of carriers remains shorter than the channel length. In graphene, the mean free path has been estimated to be in the 10-100 nm range¹⁵ so shorter channel lengths may lead to a transition to the ballistic transport regime. The ballistic scenario is out of the scope of this work.

We present here a brief account of the self-consistent simulator used to calculate the electrical behavior of GFETs. Details can be found thoroughly described in ref. 11. Upon application of the bias voltages to the different electrodes (V_{gs} , V_{ds} and V_{bs}), a sheet charge density $\sigma_{\text{free}}(y) = q[p(y) - n(y)]$ is induced in the graphene sheet. Here, p and n are the hole and electron concentration in graphene, q is the elementary charge and y is the axis that goes from source ($y = 0$) to drain ($y = L$), where L is the channel length. This charge distribution is needed in turn to calculate the electrostatic potential $\psi(x,y)$ inside the GFET (x is the position along the axis from back to top gate, see Fig. 1b). Assuming that the GFET width W (in the z direction) is large as compared with the other dimensions of the device, the Poisson's equation must be solved in the 2D domain depicted in Fig. 1b and can be written as follows:

$$\nabla \cdot [\varepsilon_r(x, y)\varepsilon_0 \nabla \psi(x, y)] = \rho_{\text{free}}(x, y) \quad (1)$$



where ε_0 is the vacuum dielectric constant, and $\varepsilon_r(x,y)$ is the relative dielectric constant, which is equal to ε_t and ε_b inside the top and back dielectrics, respectively, and ε_G in graphene. In Fig. 1b, the parameters t_t and t_b correspond to the top and the back insulator thicknesses, respectively. The charge density $\rho_{\text{free}}(x,y)$ is zero inside both dielectrics so its only contribution corresponds to $\sigma_{\text{free}}(y)$ inside graphene. When solving the Poisson's equation,

the electrostatic potential on the top gate and back gate is set to $V_{gs} - V_{gs0}$ and $V_{bs} - V_{bs0}$, respectively.¹⁶ V_{gs0} and V_{bs0} are the flatband voltages corresponding to both gates. Homogeneous Neumann's conditions are applied to the other two boundaries to ensure charge neutrality.¹⁷

The drift-diffusion equation for the drain current I_{ds} reads as follows:

$$I_{ds} = qW[n(y) + p(y)]\mu(y) \frac{dV}{dy} \quad (2)$$

where $\mu(y)$ is the mobility of electrons and holes, and $V(y)$ is the quasi-Fermi potential in the graphene. The boundary conditions make $V(y)$ to be zero at $y=0$ and V_{ds} at $y=L$. Electron and holes share the same quasi-Fermi level due to a very short recombination time of carriers in graphene, of around 10 - 100 ns.^{18,19}

From the linear dispersion relation of graphene,²⁰ the carrier concentrations are calculated by the following equations from both the electrostatic and quasi-Fermi potentials:^{11,21}

$$n(y) = \frac{n_{\text{puddle}}}{2} + N_G \mathcal{F}_1 \left[q \frac{\psi(0,y) - V(y)}{kT} \right] \quad (3a)$$

$$p(y) = \frac{n_{\text{puddle}}}{2} + N_G \mathcal{F}_1 \left[q \frac{V(y) - \psi(0,y)}{kT} \right] \quad (3b)$$

We have added to the carrier concentrations the contribution of graphene puddles n_{puddle} .²² Here, k is the Boltzmann constant, T is the temperature (which is taken to be 300 K) and N_G is the effective density of states of graphene, given by:

$$N_G = \frac{2}{\pi} \left(\frac{kT}{\hbar v_F} \right)^2 \quad (4)$$

being \hbar the reduced Planck's constant and v_F the Fermi velocity (10^8 cm s⁻¹). In eqn (3), $F_1(x)$ refers to the first order Fermi-Dirac integral:

$$\mathcal{F}_i(x) = \frac{1}{\Gamma(i+1)} \int_0^\infty \frac{u^i du}{1+e^{u-x}} \quad (5)$$

The high field mobility model that we have used in this work includes saturation velocity effects in the following form:

$$\mu = \frac{\mu_{LF}}{\left\{1 + \left| \frac{\mu_{LF} \partial \psi}{v_{sat} \partial y} \right|^\beta \right\}^{\frac{1}{\beta}}} \quad (6)$$

where the parameter β is roughly 2 for both electrons and holes, consistently with experiments.²³ By the same token, both the low-field carrier mobility μ_{LF} and saturation velocity v_{sat} have been extracted by the Monte Carlo methodology discussed in section 2.2.

In summary, given the set of materials and geometry of the GFET, and after setting the bias point (V_{gs} , V_{bs} and V_{ds}), the simulator solves in a self-consistent way the drift-diffusion transport equation (eqn (2)) coupled with the 2D Poisson's equation (eqn (1)). The simulator obtains the stationary values of I_{ds} , $n(y)$, $p(y)$, $\psi(x,y)$ and $V(y)$ as the outputs.

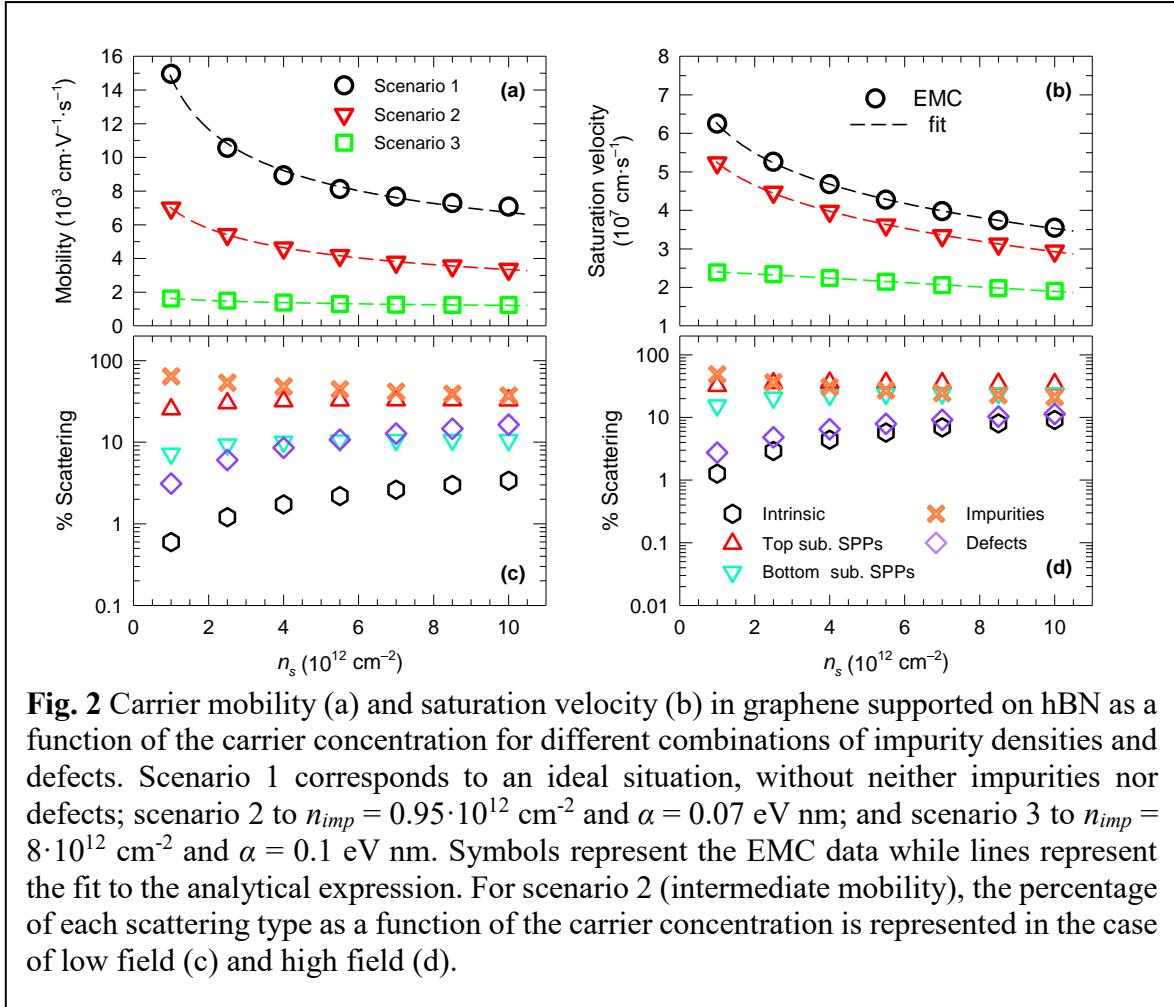
2.2 Scattering mechanisms and carrier transport properties from Monte Carlo simulations

The values of μ_{LF} and v_{sat} as a function of the carrier density have been obtained for different levels of impurities and defects in graphene by means of an EMC simulator.^{12,13} The model includes optical and acoustic intravalley phonons, electron-electron interactions, impurity scattering and scattering with defects, together with scattering with remote surface polar phonons (SPP) from the substrates. In the case of acoustic and optical phonons the scattering rates are obtained according to the deformation potential approximation,²⁴ fitting the parameters to reproduce the rates provided by the first-principles density functional theory.²⁵ Short range carrier-carrier interactions are implemented by considering a static

Coulomb screened potential model.²⁶ Impurity scattering is derived from the 2D Fourier transform of the electrostatic potential with charged centers.²⁷ Regarding graphene defects, both point defects and dislocations are considered as a single scattering mechanisms thanks to the approximation described in ref. 28 with a defect parameter α accounting for the average defect potential, the effective potential range and the density of defects. Both α and the density of impurities n_{imp} were taken as fitting parameters to reproduce the experimental mobility. The model allows for the Pauli Exclusion Principle to treat the effect of degeneracy. From the point of view of these EMC simulations, the graphene layer is placed between the top and the bottom dielectrics. The influence of the top gate metal (separated from the graphene layer by a relatively thin dielectric of thickness t_l) on the screening of impurities, remote phonons and carrier-carrier scattering has been incorporated by modifying the dielectric function with a suitable Green function.^{29,30} On the other hand, the bottom substrate is considered thick enough so that the effects on screening on the back gate can be neglected.

The number of simulated carriers ranged from 10^5 to 10^6 depending on the carrier concentration, and the time step considered in the simulation to update the distribution functions for the self-consistent treatment of the Pauli Exclusion Principle equaled 2.5 fs. The saturation velocity was determined at 20 kV cm^{-1} , as done by other authors in experimental works.²³ From the velocity-field curves obtained from the EMC simulation it is possible to extract μ_{LF} and v_{sat} as a function of the carrier concentration n_s . Different scenarios defined by the parameters α and n_{imp} have been considered. Specifically, we have assumed three levels of graphene quality referred in this work as the high mobility scenario, the intermediate mobility scenario and the low mobility scenario corresponding to scenarios 1, 2 and 3 in Fig. 2a and 2b, respectively. In order to reproduce the experimental extracted

mobility (close to $1500 \text{ cm}^2 \text{ V}^{-1} \text{ s}^{-1}$) of our experimental devices, we used a n_{imp} of $8 \cdot 10^{12} \text{ cm}^{-2}$ and α equal to 0.10 eV nm , corresponding to the low mobility scenario. The extracted mobility is also similar to that reported in ref. 28. The combination of α and n_{imp} of the intermediate mobility scenario represents the fitting to experimental mobility data for graphene on SiO_2 ,²³ and is included for comparison purposes (an improved quality sample in a realistic case). We also include an ideal scenario where neither impurities nor defects are present, which defines the best possible graphene quality.



The EMC results allow determining which scattering mechanism becomes more critical to establish the values of μ_{LF} and v_{sat} . As an example, the percentage of scattering mechanisms

is shown in Fig. 2c-d for the intermediate mobility scenario; the results for the extreme mobility cases are also shown in ESI section 1. In the low mobility scenario, the dominant scattering type are impurities, with a secondary role of defects at high carrier concentrations. Scattering with SPP from the top oxide is also relevant, particularly at large n_s , having more importance in setting the saturation velocity value. In the intermediate mobility scenario, impurities are still dominant at low fields, but interactions with the top and bottom dielectrics play an increasingly important role, especially at high electric fields, for which they can even become the primary scattering type. Finally, in the ideal case the low field mobility and saturation velocity are mainly influenced by interactions with SPP of the top (primarily) and bottom dielectrics, with progressive larger influence of intrinsic phonons at high carrier concentrations.

Once that the EMC data for μ_{LF} and v_{sat} in each scenario are obtained, the information must be introduced in the self-consistent GFET simulator. Both μ_{LF} and v_{sat} vs. n_s have been fitted to different mathematical expressions, as explained in ESI section 2. In this way, the effect on the RF performance of the scattering activity affecting electron transport can be readily evaluated.

2.3 Charge-conserving small-signal model of GFET and derived RF performance

In order to assess the RF performance of the GFET, the device can be conveniently considered as a two-port network in the common source configuration, as depicted in Fig. 3a. At the input port, a small-signal alternate current (AC) voltage source v_s , of internal admittance Y_s , transfers power and current to the network, being both v_s and Y_s complex numbers (phasors). A load admittance Y_L is connected at the output to get the transferred power. A small-signal model in form of an admittance matrix Y describes the behavior of the

two-port network and its analysis provides both the device RF performance and stability information. The small-signal parameters y_{ij} of Y can be extracted from the linearization of DC characteristics (I_{ds} and the charge controlled by the gate, source and drain terminals: Q_G , Q_S and Q_D , respectively). The Y -parameters are frequency dependent and might also strongly depend on the bias point: V_{gs} and V_{ds} . A full justification of the high frequency model can be found in ref. 31.

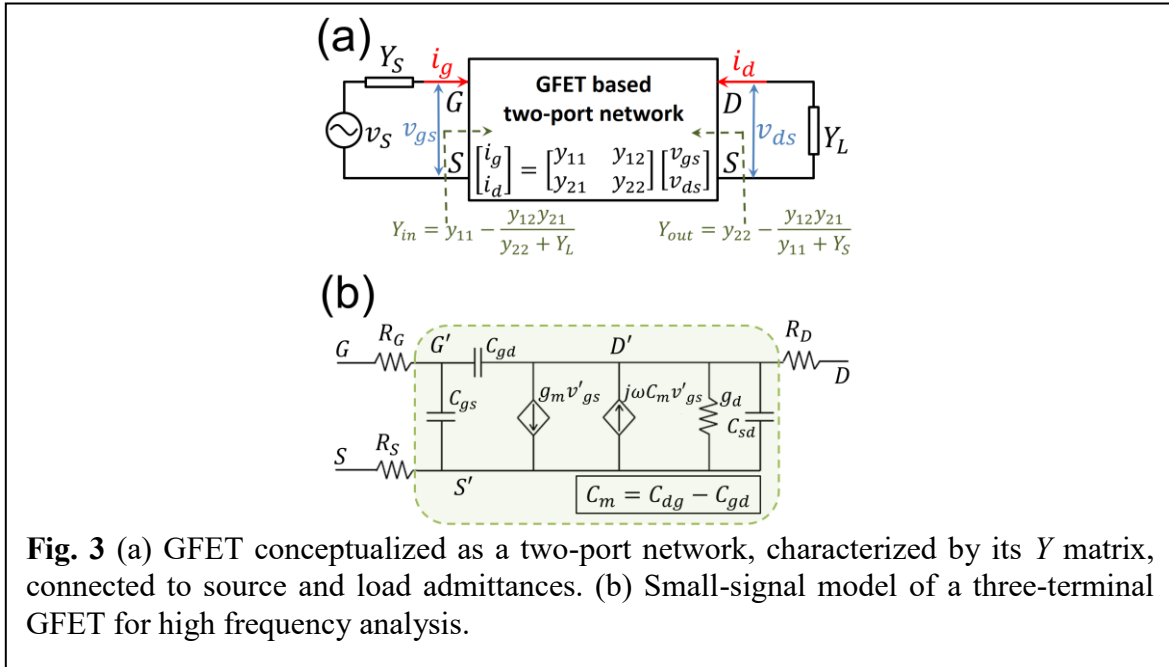


Fig. 3 (a) GFET conceptualized as a two-port network, characterized by its Y matrix, connected to source and load admittances. (b) Small-signal model of a three-terminal GFET for high frequency analysis.

A charge control model is needed to determine the small-signal parameters. We assume here that the back gate has a negligible influence over the graphene charge, which is reasonable if the back gate capacitance is much smaller than the top gate capacitance. The charges Q_S , Q_D and Q_G can be obtained from the self-consistent simulator after evaluation of the sheet charge distribution $\sigma_{free}(y)$. Upon application of a Ward-Dutton's linear charge partition scheme, the terminal charges read as:³²

$$Q_D = W \int_0^L \frac{y}{L} \sigma_{free}(y) dy \quad (7a)$$

$$Q_S = W \int_0^L \left(1 - \frac{y}{L}\right) \sigma_{\text{free}}(y) dy \quad (7b)$$

$$Q_G = -W \int_0^L \sigma_{\text{free}}(y) dy \quad (7c)$$

Notice that the total charge in the device is zero, so the model is charge-conserving. From the charge model described above, the intrinsic capacitances can be determined in the following way:

$$C_g = \left. \frac{\partial Q_G}{\partial V_{gs}} \right|_{V_{ds}} \quad (8a)$$

$$C_{dg} = - \left. \frac{\partial Q_D}{\partial V_{gs}} \right|_{V_{ds}} \quad (8b)$$

$$C_{sd} = - \left. \frac{\partial Q_S}{\partial V_{ds}} \right|_{V_{gs}} \quad (8c)$$

$$C_{gd} = - \left. \frac{\partial Q_G}{\partial V_{ds}} \right|_{V_{gs}} \quad (8d)$$

$$C_{gs} = C_g - C_{gd} \quad (8e)$$

To complete the model, the transconductance g_m and output conductance g_d need to be evaluated.

$$g_m = \left. \frac{\partial I_{ds}}{\partial V_{gs}} \right|_{V_{ds}} \quad (9a)$$

$$g_d = \left. \frac{\partial I_{ds}}{\partial V_{ds}} \right|_{V_{gs}} \quad (9b)$$

The intrinsic small-signal model of the GFET, within the shaded region of Fig. 3b, is suitable for high frequency analysis.^{31,33} A distinctive feature of this model is that no *a priori* assumption on the reciprocity of intrinsic capacitances has been made. This kind of

assumptions are usually made for silicon transistors and have often been imported directly to GFET intrinsic capacitance modeling.^{34–37} In our opinion, this practice is not well justified and important deviations of the calculated RF FoMs has been reported in ref. 38.

The intrinsic admittance matrix then takes the form:

$$Y'(\omega) = \begin{bmatrix} j\omega C_g & -j\omega C_{gd} \\ g_m - j\omega C_{dg} & g_d + j\omega(C_{gd} + C_{sd}) \end{bmatrix} \quad (10)$$

where $\omega = 2\pi f$ and f is the working frequency. To obtain the extrinsic admittance matrix we must include the influence of the series resistances of the gate, source and drain terminals (R_G , R_S and R_D , respectively). The relation between the extrinsic AC small-signal voltages v_{gs} and v_{ds} and the intrinsic ones, v'_{gs} and v'_{ds} , can be written as:

$$v_{gs} = v'_{gs} + i_g(R_G + R_S) + R_S i_d \quad (11a)$$

$$v_{ds} = v'_{ds} + R_S i_g + i_d(R_D + R_S) \quad (11b)$$

The phasors i_d and i_g are, respectively, the output and the input small-signal currents of the two-port network as defined in Fig. 3a. Then, we define the series resistance matrix Z_c as:

$$Z_c = \begin{bmatrix} R_G + R_S & R_S \\ R_S & R_D + R_S \end{bmatrix} \quad (12)$$

The final admittance matrix can be calculated by means of the following relation:

$$Y(\omega) = \{[Y'(\omega)]^{-1} + Z_c\}^{-1} \quad (13)$$

The RF FoMs can be extracted from this matrix Y . The extrinsic cutoff frequency $f_{t,x}$ is defined from the current gain, defined as $\beta(\omega) = -i_d / i_g$. The magnitude of $\beta(\omega)$ presents a maximum value when the output is shorted ($|Y_L| \rightarrow \infty$) and its expression takes the following form:³⁹

$$\beta_{max}(\omega) = \frac{-y_{21}}{y_{11}} \quad (14)$$

By definition, $f_{T,x}$ is the frequency at which the current gain is equal to one, that can be written as:

$$|\beta_{max}(2\pi f_{T,x})| = 1 \quad (15)$$

Before discussing the procedure to get f_{max} , we must recall the concept of stability of a general two-port amplifier circuit in terms of the Y -parameters of a transistor. Stability guarantees that no adventitious oscillations can appear at a network for any passive source and load admittances connected to the input and output ports, respectively. This requires that the reflection coefficients of the input and output ports are smaller than one. Equivalently, the stability of a network can be assessed by means of the K - Δ test, which is based on the evaluation of the two following factors:³⁹

$$K(\omega) = \frac{2 \operatorname{Re}(y_{11}) \operatorname{Re}(y_{22}) - \operatorname{Re}(y_{12}y_{21})}{|y_{12}y_{21}|} \quad (16a)$$

$$\Delta(\omega) = \frac{(Y_0 - y_{11})(Y_0 - y_{22}) - y_{12}y_{21}}{(Y_0 + y_{11})(Y_0 + y_{22}) - y_{12}y_{21}} \quad (16b)$$

where $Y_0 = 1/Z_0$ is the characteristic admittance and Z_0 is the characteristic impedance (usually taken as 50 Ω). Both conditions $K > 1$ and $|\Delta| < 1$ are necessary and sufficient to ensure device stability. In this case, any passive load and input admittance provide a stable behavior of the network. Selecting an optimum set of Y_S and Y_L , an optimized power gain can be obtained, referred as the maximum available gain (MAG). However, if $-1 < K < 1$, the network is said to be conditionally stable, that is, it becomes stable only for certain combinations of Y_S and Y_L . Among those combinations that provide stability, the maximum attainable power gain is known as the maximum stable gain (MSG). Therefore, the maximum

gain $|G(\omega)|_{max}$ can be calculated from Y and it depends on the value of the stability factor K following these relations:

$$|G(\omega)|_{max} = \begin{cases} MAG = \left| \frac{y_{21}}{y_{12}} \right| (K - \sqrt{K^2 - 1}) & K \geq 1; |\Delta| < 1 \\ MSG = \left| \frac{y_{21}}{y_{12}} \right| & -1 < K < 1 \end{cases} \quad (17)$$

Once $G(\omega)$ has been defined, f_{max} can be calculated as follows:

$$|G(2\pi f_{max})|_{max} = 1 \quad (18)$$

2.4 Fabrication and measurement of GFETs

The hBN flakes were prepared by mechanical exfoliation on SiO₂/Si substrate. To fabricate a GFET, graphene grown by photo-thermal chemical vapor deposition⁴⁰ was transferred onto the hBN and, subsequently, was patterned with oxygen plasma to define the graphene channel. Ti/Au (2/50 nm) metal electrodes were contacted to the graphene channel utilizing lift-off technique. Afterwards, 26-nm-thick Al₂O₃ was deposited on the top surface of the structure for a dielectric layer. A second layer graphene was transferred on the dielectric layer and patterned for a gate electrode. Finally, Ti/Au metal lead for a gate was fabricated. All DC measurements were performed at room temperature using semiconductor parameter analyzer (HP4155A) in ambient conditions.

3. Results and discussions

3.1 Comparison with experimental values

We have checked the predictive behavior of the self-consistent simulator by comparing its outcome with experimental I-V curves of a GFET. The graphene channel is on the top of a layer of hBN with a thickness of the order of tens of nm, which is placed on 285 nm thick SiO₂. An atomic force microscopy (AFM) image of the device and its structure layout

including the hBN flake are shown in Fig. 4a and 4b, respectively. A 26 nm Al_2O_3 layer was grown by atomic layer deposition on top of the graphene layer as top gate insulator. For simulation purposes, we have considered the parameters of the GFET presented in Table 1. The source and drain contact resistances have been assumed as one fitting parameter, $R_S = R_D$, to optimize the agreement between the model outcome and the experiment. Note that the contact resistance is sensitive to the back gate voltage since graphene under the source/drain contacts is overlapped with the global back gate.^{41,42} The relation between both DC intrinsic voltages (V_{gs} and V_{ds}) and extrinsic voltages ($V_{gs,ext}$ and $V_{ds,ext}$ for gate-to-source and drain-to-source, respectively) depend on drain current I_{ds} , R_S and R_D as follows:

$$V_{ds,ext} = V_{ds} + I_{ds}(R_S + R_D) \quad (19a)$$

$$V_{gs,ext} = V_{gs} + I_{ds}R_S \quad (19b)$$

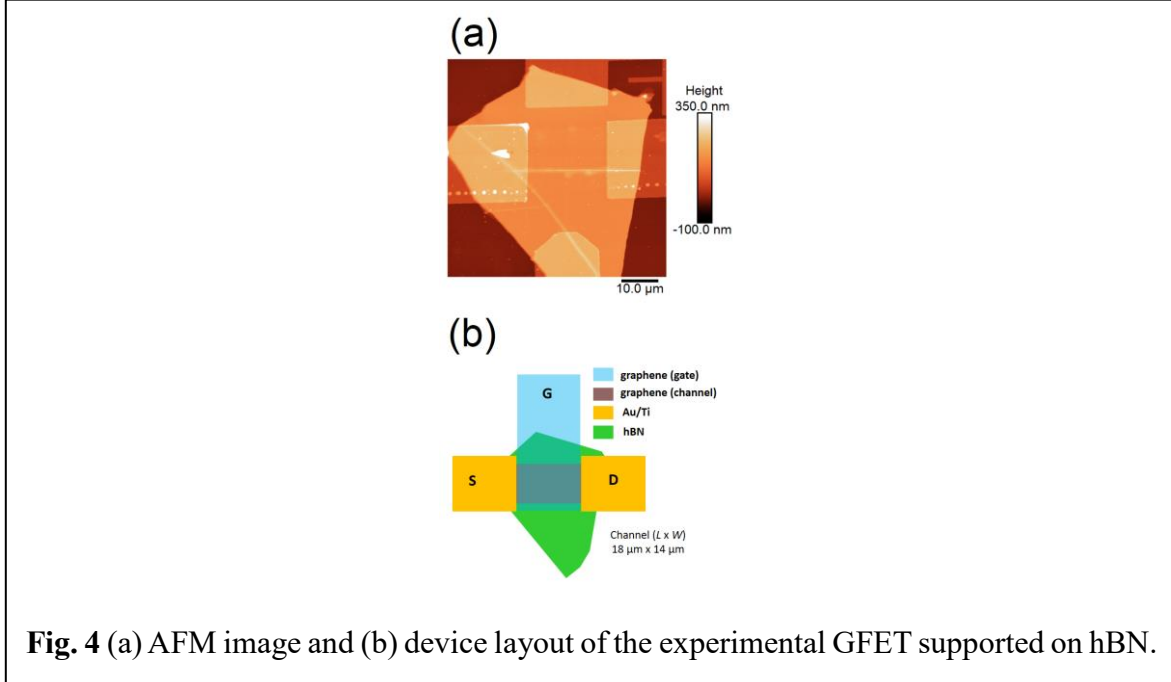
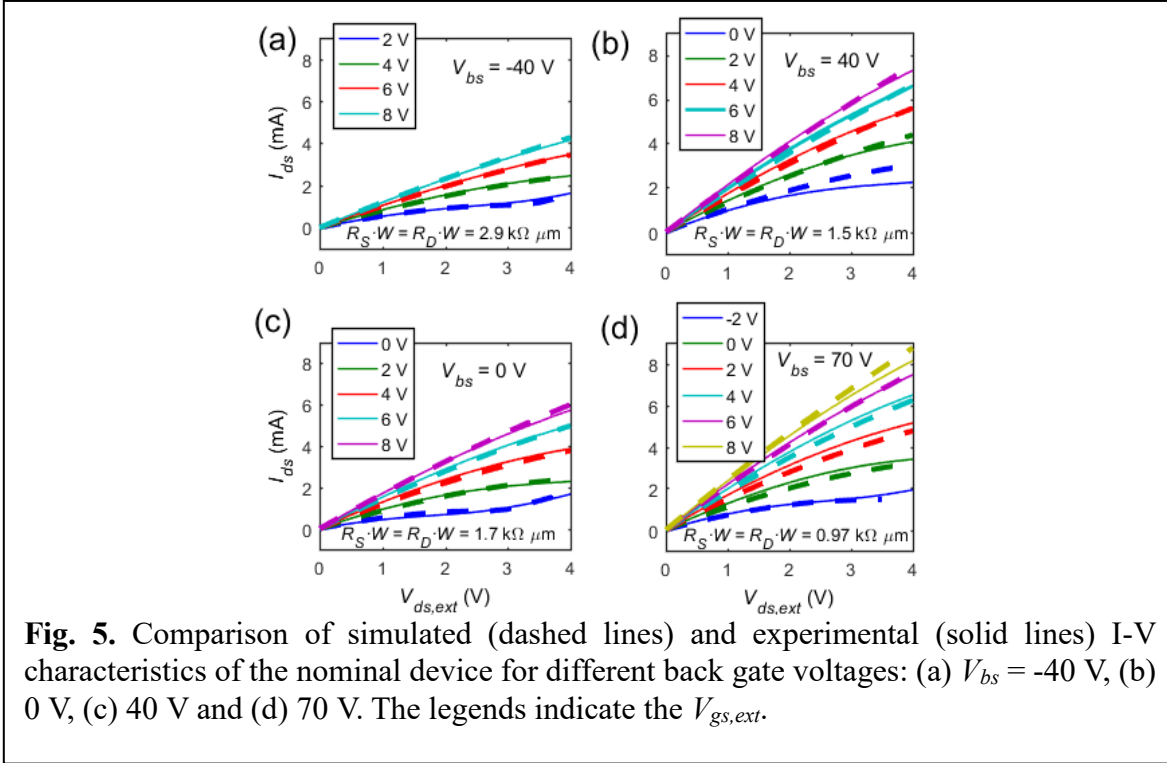


Table 1. Parameters of the nominal GFET supported on hBN used in the simulation.

Parameter	Value
L	18 μm
W	14 μm
t_t	26 nm
t_b	285 nm
ϵ_t	9
ϵ_b	3.9
V_{gs0}	-2.5 V
V_{bs0}	0 V
n_{imp}	$8 \cdot 10^{12} \text{ cm}^{-2}$
α	0.10 eV nm

Fig. 5a-d plot together the experimental and calculated curves, showing good agreement even if very different back gate voltages V_{bs} are considered. The values of the series resistances found for each V_{bs} resulted from contact resistance modulated by the back gate. A thorough discussion of this effect can be found in ref. 42 and 41. We neglected the influence of interface traps that might exist at the insulator-graphene interface. Nevertheless, in ESI section 3, we report on the impact that might exist due to the non-ideal Al_2O_3 /graphene interface⁴³ with an interface trap capacitance of 10 fF μm^{-2} . We have found that this additional capacitance, which is a realistic value, does not significantly affect the I-V characteristics nor the transcapacitances.



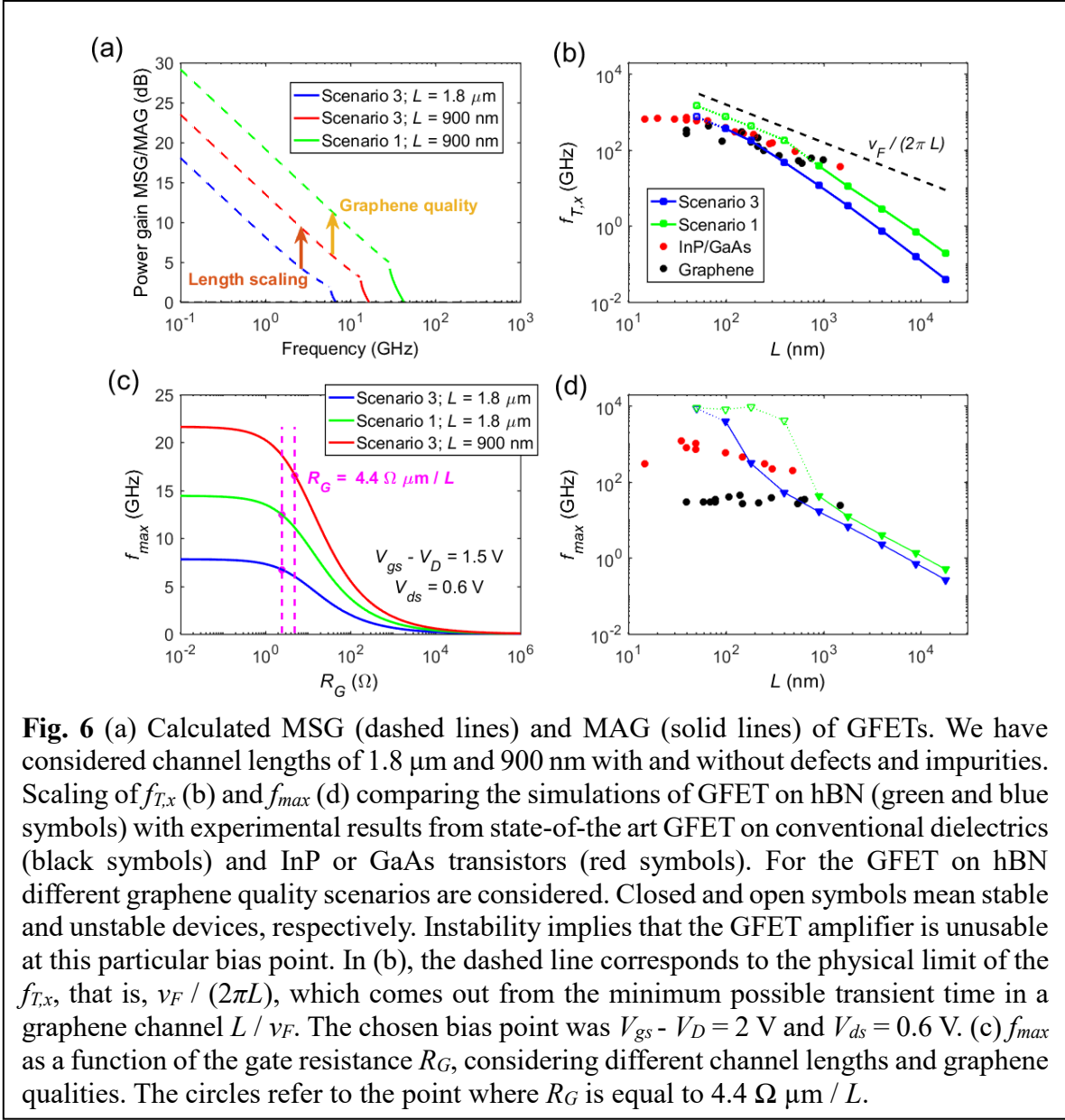
3.2 RF performance scaling and device stability

The small-signal model has been used to investigate the scalability of RF performance via channel length reduction, considering device stability at the same time. We anticipate that stability plays a vital role, especially in short-channel transistors. We have studied the effect of graphene quality for the two extreme mobility scenarios considered in the Monte Carlo simulations. The intermediate mobility scenario gives medium RF performance and its discussion would be qualitatively similar, so we have not included it for the sake of brevity. To run the simulations we have used state-of-the-art values of the source/drain series resistance $R_S \cdot W = R_D \cdot W = 200 \Omega \mu\text{m}$.⁴⁴ Regarding the gate series resistance, it was calculated considering a metal gate contacted on both sides of the device.³¹ If the GFET width is large enough, we can approximate the gate resistance to be inversely proportional to channel length. For instance, a realistic value of $R_G \cdot L$ could be $4.4 \Omega \mu\text{m}$, calculated assuming a 60 nm

thick wolfram gate (resistivity of 56 nΩ m). The increase of R_G with scaling compromises the ultimate f_{max} of GFETs so gate resistance minimization is key in RF applications.⁴⁵ Regarding the density of puddles, we have assumed it as zero for the results presented in the main text. We have not found significant deviations in the RF performances assuming densities up to $\sim 10^{11}$ cm⁻², provided that the chosen bias point is far enough from the Dirac point. A more in-depth investigation of the puddle concentration and its effects on RF performances can be found in ESI section 4.

The GFET RF performance is, in general, dependent on the bias point. For our RF investigation, we have chosen the combination $V_{ds} = 0.6$ V and $V_{gs} - V_D = 2$ V, where V_D is the Dirac voltage, so the device is biased in the region where f_{max} and $f_{T,x}$ are quite insensitive to V_{gs} (see ESI section 5). This eases the comparison with other devices since the performance does not depend so much on the bias point.

The impact of the channel length downscaling and graphene quality on the power gain can be observed in Fig. 6a. The MSG presents a slope of 10 dB dec⁻¹ for all devices, but reducing the channel length by a factor of 2 results in an increase of the power gain of 5.4 dB while f_{max} grows from 6.5 to 16 GHz. A similar improvement is achieved if the electron mobility increases from the low mobility scenario up to the highest one.



Next, we have shown in Fig. 6b,d the scaling of $f_{T,x}$ and f_{max} with L . Details on the scaling of the small-signal parameters can be found in ESI section 6. For long channel lengths ($> 1 \mu\text{m}$), $f_{T,x}$ scales as $1/L^2$. This is because g_m is proportional to $1/L$ while C_g scales as L . However, for short channel lengths ($< 1 \mu\text{m}$) the scaling law approaches $1/L$ because of saturation velocity effects, which make g_m quite insensitive to L . Increasing the graphene quality improves $f_{T,x}$ in a factor larger than 2. The numbers shown in Fig. 6b are comparable

to what has been reported value for InP and GaAs high electron mobility transistors (HEMTs), which are the highest reported value for RF transistors.² Importantly, we have found out that for short-channel devices, the device becomes unstable at very short L , especially in the high mobility scenario. This particular issue of instability will be later discussed.

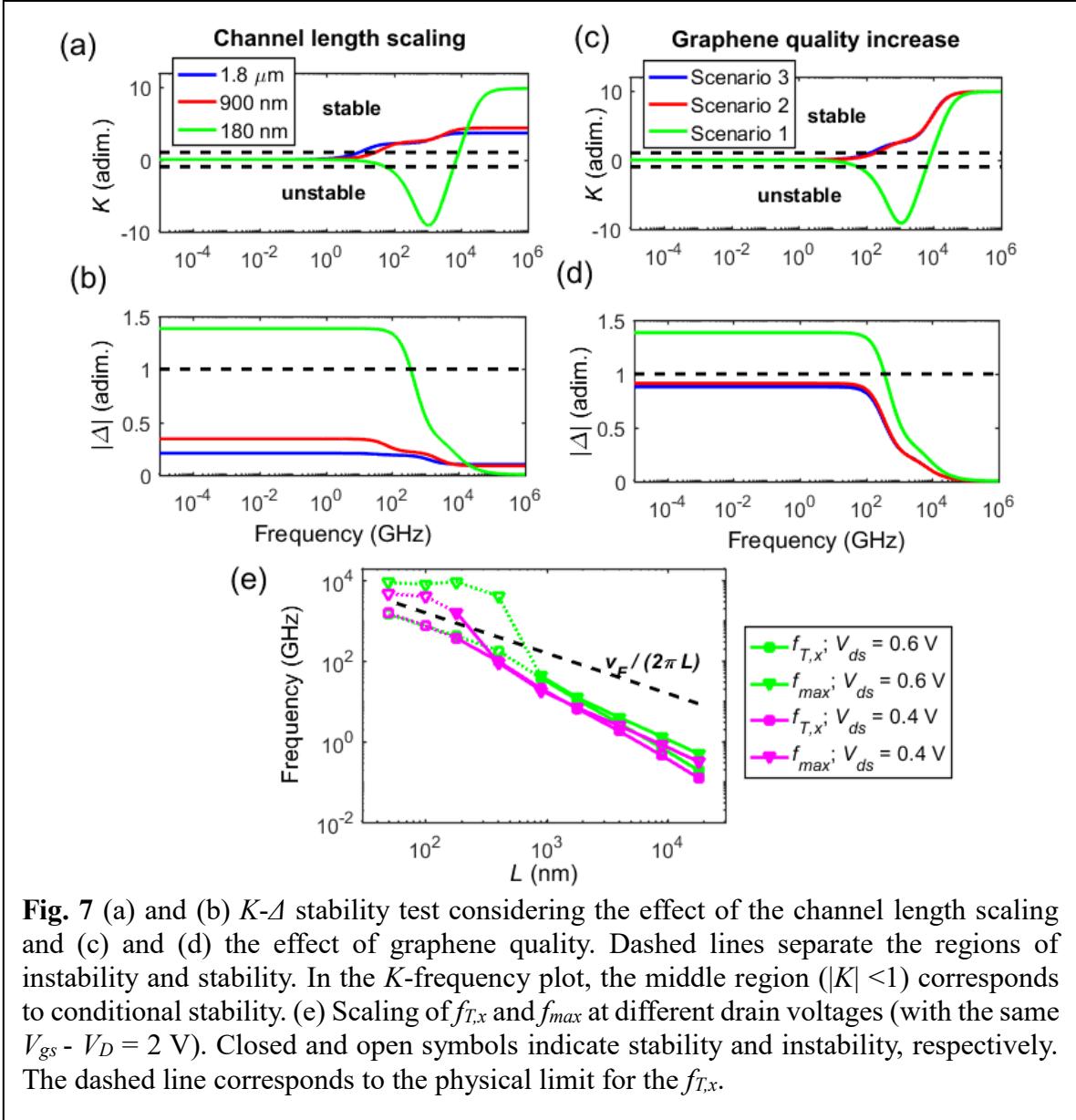
Regarding f_{max} scalability, shown in Fig. 6d, we have found a different trend to the one for $f_{T,x}$. At long channel lengths, the scaling law is $1/L^n$ with $1 < n < 2$, which is in fact a scaling power smaller than $f_{T,x}$ due to the upscaling of R_G . The increase in graphene quality slightly improves f_{max} . However, at short channel lengths ($< 1 \mu\text{m}$), there is a huge increase in f_{max} because of current saturation driven by the velocity saturation effect. Our simulations indicate the great potential that the GFET on hBN might have to push f_{max} into the THz region. Intrinsic I-V curves for different devices depending on the quality of graphene and channel length can be found in ESI section 7.

The gate series resistance is in fact an important source of RF performance degradation. Fig. 6c illustrates how f_{max} decreases with the gate series resistance. The graph compares the results for devices with different channel lengths (900 nm and 1.8 μm) and devices with different levels of graphene quality (lowest and highest mobility scenarios). It is then clear that minimizing the gate series resistance produces an important improvement in f_{max} , even more prominent when the channel becomes shorter. Besides, no relation has been found between the stability of the GFET and the gate resistance.

Let us turn now the attention to the device stability issue. In Fig. 7a-d we have plotted the stability factors K and $|A|$ considering different channel lengths and graphene qualities. First, we first focus on the stability of devices with different L (Fig. 7a,b). While longer devices

show conditional stability, the factor K in the short channel case ($L = 180$ nm) decreases below -1 for a set of frequencies between $\sim 10^2$ and 10^4 GHz. The scaled transistor thus enters in the unstable region, which prevents it from working properly as a power amplifier. Similarly, for a fixed gate length (Fig. 7c,d), we have found that moving towards the high mobility scenario could be detrimental as the device is more prone to instability, which could imply sacrificing some power gain to restore stable RF operation. Therefore, we suggest that a low mobility scenario is helpful to extend the device stability to shorter channel lengths, although paying the prize of getting smaller RF performance. Device stability is eventually lost when the transistor with the low mobility is aggressively scaled down to 40 nm (provided that the diffusive regime was still valid).

Finally, it is relevant to analyze how the choice of the drain bias could impact on the RF performance and device stability. Fig. 7e compares $f_{T,x}$ and f_{max} as a function of the L at both $V_{ds} = 0.6$ V and $V_{ds} = 0.4$ V. For long channel lengths ($L > 1$ μm), the reduction in V_{ds} gives a slight decrease in the FoMs. However, a reduced V_{ds} can be used to extend the device stability to lower channel lengths down to 180 nm. As a result, we can conclude that the choice of the bias point is important not only to maximize $f_{T,x}$, f_{max} or the power gain but also to make sure that the device works in the stable region.



4. Conclusions

We have analyzed the electrical behavior of the GFET supported on hBN targeting RF applications. For such a purpose we have followed a multiscale approach, combining EMC simulations to evaluate the impact of scattering on electronic transport and GFET device simulations to assess the DC and RF performance. The Monte Carlo simulation (that includes the most relevant scattering mechanisms affecting carrier transport in real samples) provides

the carrier mobility and saturation velocity dependence with the carrier concentration; this information has been fed in a self-consistent simulator to get the DC characteristics. The results have been successfully compared with experimental measurements of fabricated devices. From the DC behavior, we have calculated the small-signal parameters of the GFET to study the RF performance. Then we have thoroughly studied the influence of the graphene quality and channel length scaling as possible ways to improve the RF performance. Our results indicate that the stability of a GFET is an important factor that could prevent the device from being usable. We have found that short-channel GFETs with very high mobility could be unstable, so care must be exercised when designing the device. Moreover, the choice of the bias point is critical to guarantee a stable operation. Finally, we have proved that increasing f_{max} would require a minimization of the gate series resistance to get competitive FoMs, especially for short-channel devices.

Acknowledgements

We acknowledge the provision of facilities and technical support by Aalto University at Micronova Nanofabrication Centre for GFET fabrication. This work is funded by the European Union's Horizon 2020 research and innovation program (grant agreement No 696656), the *Ministerio de Economía y Competitividad* (projects TEC2013-42622-R, TEC2015-67462-C2-1-R, TEC2016-80839-P, MINECO/FEDER and grant FJCI-2014-19643), the *Ministerio de Educación* (CAS16/00043) and the *Generalitat de Catalunya* (project 2014 SGR 384).

References

- 1 F. Schwier, R. Granzner and J. Pezoldt, *Nanoscale*, 2015, **7**, 8261–8283.

- 2 F. Schwierz, *Proc. IEEE*, 2013, **101**, 1567–1584.
- 3 H. Wang, A. Hsu and J. Kong, *IEEE Trans. Electron Devices*, 2011, **58**, 1523–1533.
- 4 K. S. Novoselov, a K. Geim, S. V Morozov, D. Jiang, M. I. Katsnelson, I. V Grigorieva, S. V Dubonos and a a Firsov, *Nature*, 2005, **438**, 197–200.
- 5 K. I. Bolotin, K. J. Sikes, J. Hone, H. L. Stormer and P. Kim, *Phys. Rev. Lett.*, 2008, **101**, 1–4.
- 6 G. López-Polín, C. Gómez-Navarro, V. Parente, F. Guinea, M. I. Katsnelson, F. Pérez-Murano and J. Gómez-Herrero, *Nat. Phys.*, 2014, **11**, 26–31.
- 7 I. W. Frank and D. M. Tanenbaum, *J. Vac. Sci. Technol. B Microelectron. Nanom. Struct.*, 2007, **25**, 2558–2561.
- 8 N. Petrone, I. Meric, T. Chari, K. L. Shepard and J. Hone, *IEEE J. Electron Devices Soc.*, 2015, **3**, 44–48.
- 9 C. R. Dean, A. F. Young, I. Meric, C. Lee, L. Wang, S. Sorgenfrei, K. Watanabe, T. Taniguchi, P. Kim, K. L. Shepard and J. Hone, *Nat. Nanotechnol.*, 2010, **5**, 722–726.
- 10 I. Meric, C. R. Dean, N. Petrone, L. Wang, J. Hone, P. Kim and K. L. Shepard, *Proc. IEEE*, 2013, **101**, 1609–1619.
- 11 P. C. Feijoo, D. Jiménez and X. Cartoixà, *2D Mater.*, 2016, **3**, 1–13.
- 12 R. Rengel and M. J. Martín, *J. Appl. Phys.*, 2013, **114**, 143702.
- 13 R. Rengel, E. Pascual and M. J. Martín, *Appl. Phys. Lett.*, 2014, **104**, 233107.
- 14 Y. Wu, X. Zou, M. Sun, Z. Cao, X. Wang, S. Huo, J. Zhou, Y. Yang, X. Yu, Y. Kong, G. Yu, L. Liao and T. Chen, *ACS Appl. Mater. Interfaces*, 2016, **8**, 25645–25649.

- 15 W. Zhu, V. Perebeinos, M. Freitag and P. Avouris, *Phys. Rev. B - Condens. Matter Mater. Phys.*, 2009, **80**, 235402.
- 16 D. Jiménez, *Appl. Phys. Lett.*, 2012, **101**, 243501.
- 17 V. Mishra, S. Smith, L. Liu, F. Zahid, Y. Zhu, H. Guo and S. Salahuddin, *IEEE Trans. Electron Devices*, 2015, **62**, 2457–63.
- 18 F. Rana, *Phys. Rev. B*, 2007, **76**, 155431.
- 19 F. Rana, P. A. George, J. H. Strait, J. Dawlaty, S. Shivaraman, M. Chandrashekar and M. G. Spencer, *Phys. Rev. B - Condens. Matter Mater. Phys.*, 2009, **79**, 115447.
- 20 A. H. Castro Neto, F. Guinea, N. M. R. Peres, K. S. Novoselov and A. K. Geim, *Rev. Mod. Phys.*, 2009, **81**, 109–162.
- 21 J. G. Champlain, *J. Appl. Phys.*, 2011, **109**, 84515.
- 22 J. Martin, N. Akerman, G. Ulbricht, T. Lohmann, J. H. Smet, K. von Klitzing and A. Yacoby, *Nat. Phys.*, 2007, **4**, 144–148.
- 23 V. E. Dorgan, M. H. Bae and E. Pop, *Appl. Phys. Lett.*, 2010, **97**, 8–11.
- 24 E. H. Hwang and S. Das Sarma, *Phys. Rev. B - Condens. Matter Mater. Phys.*, 2008, **77**, 1–6.
- 25 K. M. Borysenko, J. T. Mullen, E. A. Barry, S. Paul, Y. G. Semenov, J. M. Zavada, M. B. Nardelli and K. W. Kim, *Phys. Rev. B - Condens. Matter Mater. Phys.*, 2010, **81**, 3–6.
- 26 X. Li, E. A. Barry, J. M. Zavada, M. B. Nardelli and K. W. Kim, *Appl. Phys. Lett.*, 2010, **97**, 10–13.

- 27 S. Adam, E. H. Hwang, E. Rossi and S. Das Sarma, *Solid State Commun.*, 2009, **149**, 1072–1079.
- 28 D. K. Ferry, *J. Comput. Electron.*, 2013, **12**, 76–84.
- 29 Z. Y. Ong and M. V. Fischetti, *Phys. Rev. B - Condens. Matter Mater. Phys.*, 2012, **86**, 1–4.
- 30 Z. Y. Ong and M. V. Fischetti, *Phys. Rev. B - Condens. Matter Mater. Phys.*, 2013, **88**, 1–18.
- 31 Y. Tsividis and C. McAndrew, *The MOS transistor*, Oxford University Press, New York, Third Edit., 2012.
- 32 D. E. Ward and R. W. Dutton, *IEEE J. Solid-State Circuits*, 1978, **13**, 703–708.
- 33 K. D. Holland, N. Paydavosi, N. Neophytou, D. Kienle and M. Vaidyanathan, *IEEE Trans. Nanotechnol.*, 2013, **12**, 566–577.
- 34 S. Rodriguez, S. Vaziri, A. Smith, S. Fregonese, M. Ostling, M. C. Lemme and A. Rusu, *IEEE Trans. Electron Devices*, 2014, **61**, 1199–1206.
- 35 O. Habibpour, J. Vukusic and J. Stake, *IEEE Trans. Electron Devices*, 2012, **59**, 968–975.
- 36 J. G. Champlain, *Solid. State. Electron.*, 2012, **67**, 53–62.
- 37 G. I. Zebrev, A. A. Tselykovskiy, D. K. Batmanova and E. V. Melnik, *IEEE Trans. Electron Devices*, 2013, **60**, 1799–1806.
- 38 F. Pasadas, W. Wei, E. Pallecchi, H. Happy and D. Jiménez,
<https://arxiv.org/ftp/arxiv/papers/1704/1704.00181.pdf>.

- 39 D. M. Pozar, *Microwave Engineering*, John Wiley & Sons, INC, Hoboken, NJ, Forth., 2012.
- 40 J. Riikonen, W. Kim, C. Li, O. Svensk, S. Arpiainen, M. Kainlauri and H. Lipsanen, *Carbon N. Y.*, 2013, **62**, 43–50.
- 41 F. A. Chaves, D. Jiménez, A. A. Sagade, W. Kim, J. Riikonen, H. Lipsanen and D. Neumaier, *2D Mater.*, 2015, **2**, 25006.
- 42 F. A. Chaves, D. Jiménez, A. W. Cummings and S. Roche, *J. Appl. Phys.*, 2014, **16**, 164513.
- 43 Z. Chen and J. Appenzeller, in *IEEE International Electron Devices Meeting*, 2008, pp. 1–4.
- 44 F. Xia, V. Perebeinos, Y. Lin, Y. Wu and P. Avouris, *Nat. Nanotechnol.*, 2011, **6**, 179–184.
- 45 D. B. Farmer, A. Valdes-Garcia, C. Dimitrakopoulos and P. Avouris, *Appl. Phys. Lett.*, 2012, **101**, 2010–2013.

Electronic supporting information

Scaling of graphene field-effect transistors supported on hexagonal boron nitride: radio-frequency stability as a limiting factor

Pedro C. Feijoo^a, Francisco Pasadas^a, José M. Iglesias^b, María J. Martín^b, Raúl Rengel^b, Changfeng Li^c, Wonjae Kim^{c,d}, Juha Riikonen^c, Harri Lipsanen^c, David Jiménez^a

^a Departament d'Enginyeria Electrònica, Escola d'Enginyeria, Universitat Autònoma de Barcelona, 08193 Bellaterra, Spain

^b Departamento de Física Aplicada, Universidad de Salamanca, Salamanca 37008, Spain

^c Department of Electronics and Nanoengineering, Aalto University, 02150 Espoo, Finland

^d VTT Technical Research Center of Finland, 02150 Espoo, Finland

Section 1. Influence of the scattering types on all mobility scenarios

From the Monte Carlo data, it is possible to unravel the influence of each separate scattering type on the low field mobility and the saturation velocity. The results for the three scenarios are shown in Fig. S1, where the percentage of each scattering type is shown as a function of the carrier concentration.

In the lowest mobility case, scenario 3, the dominant mechanism is impurity scattering. As the carrier concentration grows, scattering with defects increases its weight, becoming the second interaction type together with interactions with remote surface polar phonons (SPP) from the top Al_2O_3 . At high electric field, while impurity is still the dominant scattering type, interactions with the dielectrics and intrinsic optical phonons become also relevant at high n_s .

The second mobility scenario (intermediate mobility) shows also a dominant role of impurities and interactions with SPP of the top substrate: in particular, these latter ones become the most important scattering type at medium and large carrier concentrations. With regard to the saturation velocity conditions, the interactions with the dielectrics are the most relevant scattering type at medium and large carrier concentrations.

Finally, in the highest mobility case (absence of impurities or defects) the low and high field situations are mostly dominated by the interactions with remote SPP from Al_2O_3 , although interactions with the underlying hBN are also relevant. A higher influence of intrinsic phonons is also observed as the carrier concentration increases.

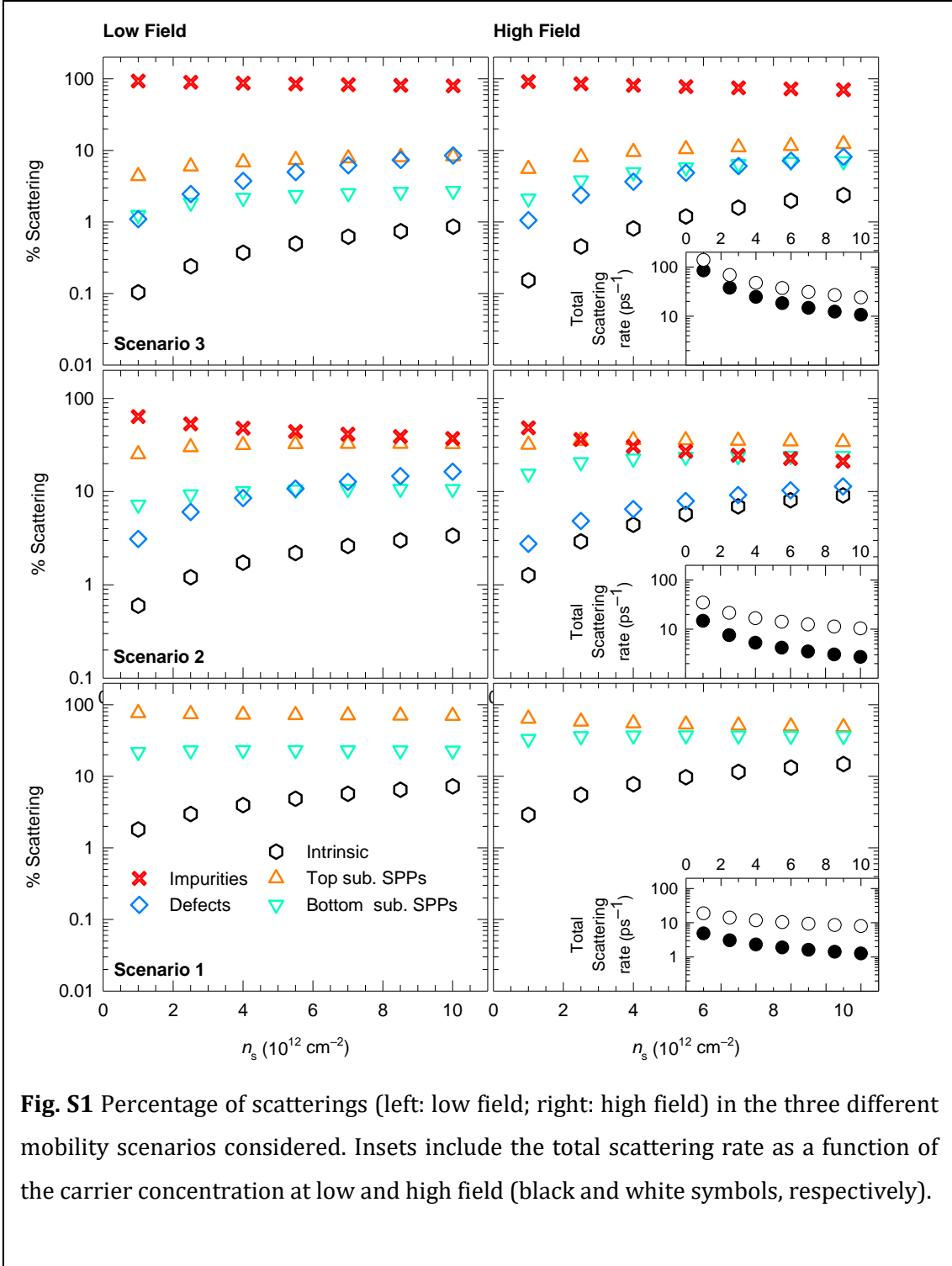


Fig. S1 Percentage of scatterings (left: low field; right: high field) in the three different mobility scenarios considered. Insets include the total scattering rate as a function of the carrier concentration at low and high field (black and white symbols, respectively).

Section 2. Analytical curves for the mobility and saturation velocity derived from Monte Carlo simulations

From the Monte Carlo data for the mobility and saturation velocity, we have fitted the results to analytical curves to be included in the GFET simulator. For this purpose, in the case of the low field mobility we considered the following expression:

$$\mu_{LF} = \frac{\mu_0}{1 + \left(\frac{n_s}{a_1}\right)^{b_1}} \quad (S1)$$

where n_s is the carrier concentration and μ_0 , a_1 , and b_1 are the fitting parameters. The fitting has been made in the $5 \cdot 10^{11}$ - 10^{13} cm^{-2} range.

Regarding the saturation velocity, it can be fitted to a potential law of the form:

$$v_{sat} = v_{sat,0} \left(1 + a_2 \left(\frac{n_s}{n_0} \right)^{b_2} \right) \quad (S2)$$

where $v_{sat,0}$, a_2 and b_2 are the fitting parameters, and n_0 is a reference carrier concentration of 10^{12} cm^{-2} . The whole set of fitting parameters for the three scenarios are summarized in Table S1, and the results are shown in Fig. 2a,b in the main text.

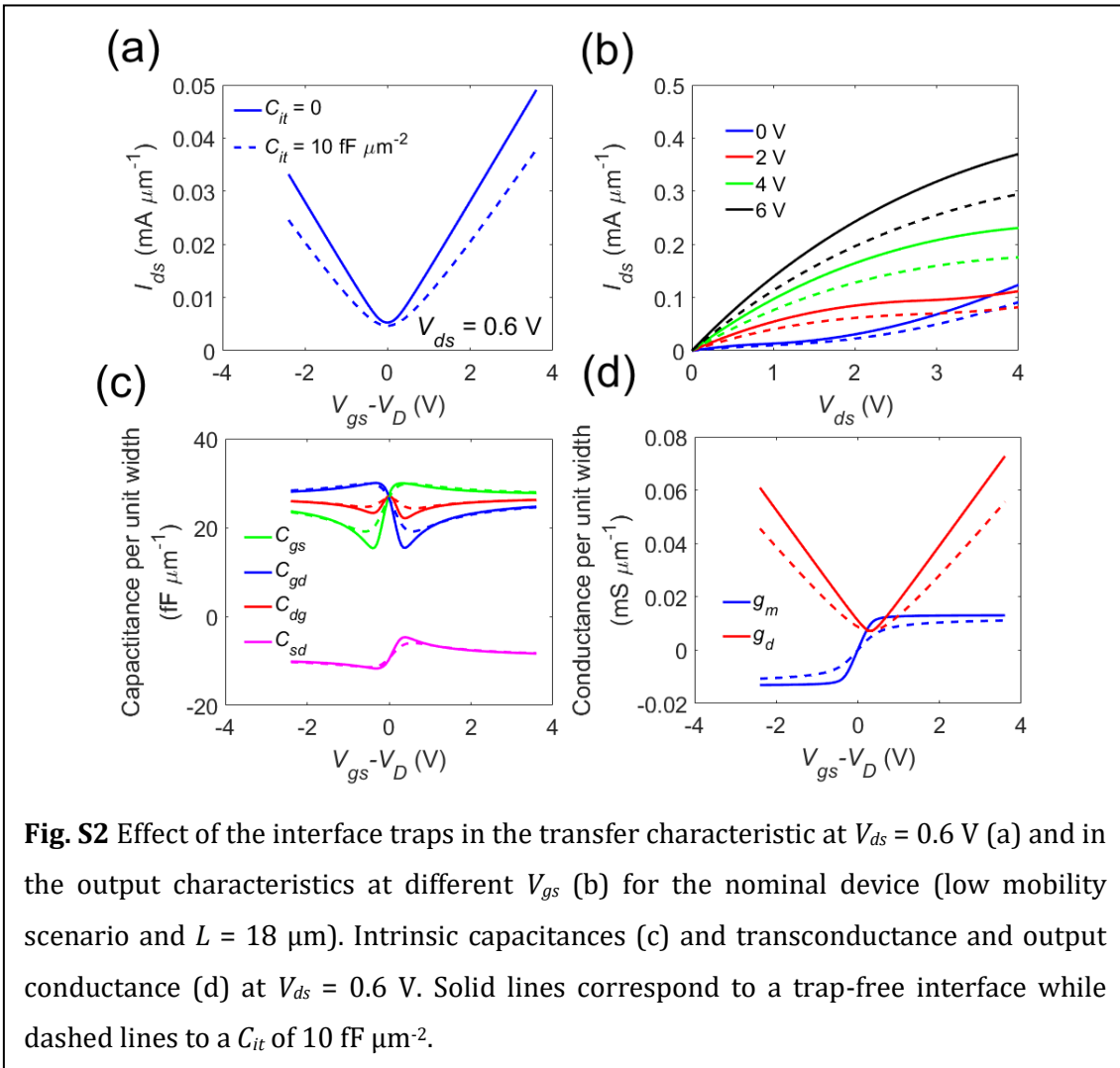
Below a minimum carrier concentration of $5 \cdot 10^{11}$ cm^{-2} , both μ_{LF} and v_{sat} have been considered to be constant, taking the value of both magnitudes at $5 \cdot 10^{11}$ cm^{-2} . The Monte Carlo extracted values are then used in eqn (19). The magnitudes of μ_{LF} and v_{sat} have been simulated only for the electrons; the same values have been considered for holes, considering the symmetry in the conduction and valence bands in graphene close to the Dirac point.

Table S1. Fitting parameters for electron mobility and saturation velocity to match the curves obtained from the Monte Carlo simulations.

	$n_{imp} = 8 \cdot 10^{12}$ cm^{-2} $\alpha = 0.10$ eV nm (Scenario 3, mobility corresponding to the experimental values)	$n_{imp} = 9.5 \cdot 10^{11}$ cm^{-2} $\alpha = 0.07$ eV nm (Scenario 2, improved quality realistic case)	$n_{imp} = 0$ cm^{-2} $\alpha = 0$ eV nm (Scenario 1, defect and impurity-free graphene)
μ_0	$2.4 \cdot 10^3$ $\text{cm}^2 \text{V}^{-1} \text{s}^{-1}$	$1.4 \cdot 10^4$ $\text{cm}^2 \text{V}^{-1} \text{s}^{-1}$	$3.1 \cdot 10^5$ $\text{cm}^2 \text{V}^{-1} \text{s}^{-1}$
a_1	$6.9 \cdot 10^{12}$ cm^{-2}	$2.3 \cdot 10^{11}$ cm^{-2}	$2.0 \cdot 10^8$ cm^{-2}
b_1	0.33	0.42	0.35
$v_{sat,0}$	$2.5 \cdot 10^7$ cm s^{-1}	$9.2 \cdot 10^7$ cm s^{-1}	$1.9 \cdot 10^8$ cm s^{-1}
a_2	$-6.1 \cdot 10^{-2}$	-0.43	-0.67
b_2	0.69	0.20	$8.6 \cdot 10^{-2}$

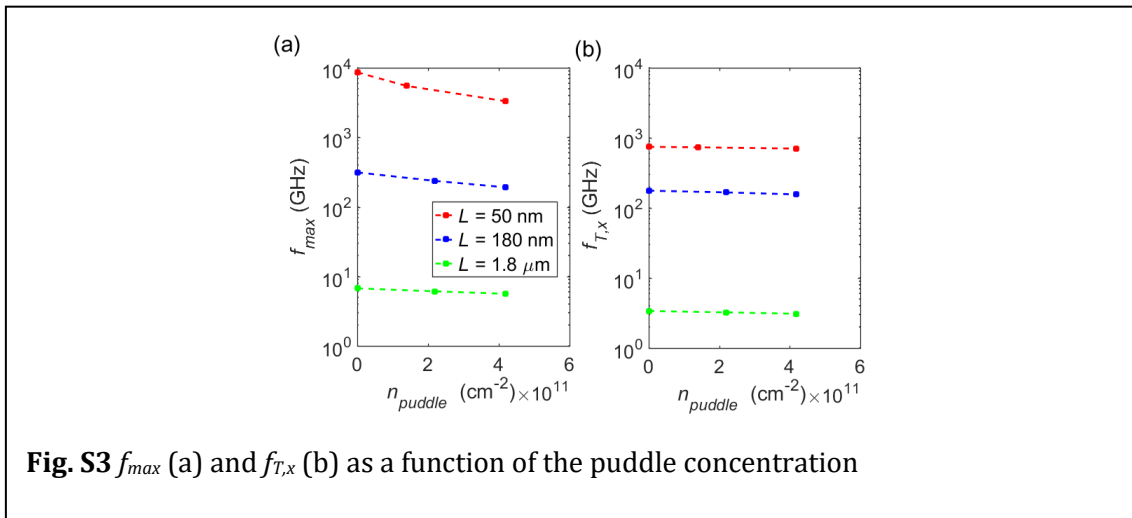
Section 3. Influence of interface traps

Although the simulated I-V curves reasonably agree with the experimental measurements, it is important to analyze the hypothetical effect that interface traps might have. Fig. S2 compares the DC curves and the small-signal parameters of a GFET free from interface traps with a device assuming an interface trap capacitance C_{it} of $10 \text{ fF } \mu\text{m}^{-2}$, which is a realistic value.¹ The traps in the graphene-dielectric interface decrease the number of carriers in the channel at a given bias, which decreases in turn the drain current and thus the transconductance and the output conductance (especially at biases that are far from the Dirac voltage). On the other hand, intrinsic capacitances barely remain unaffected.



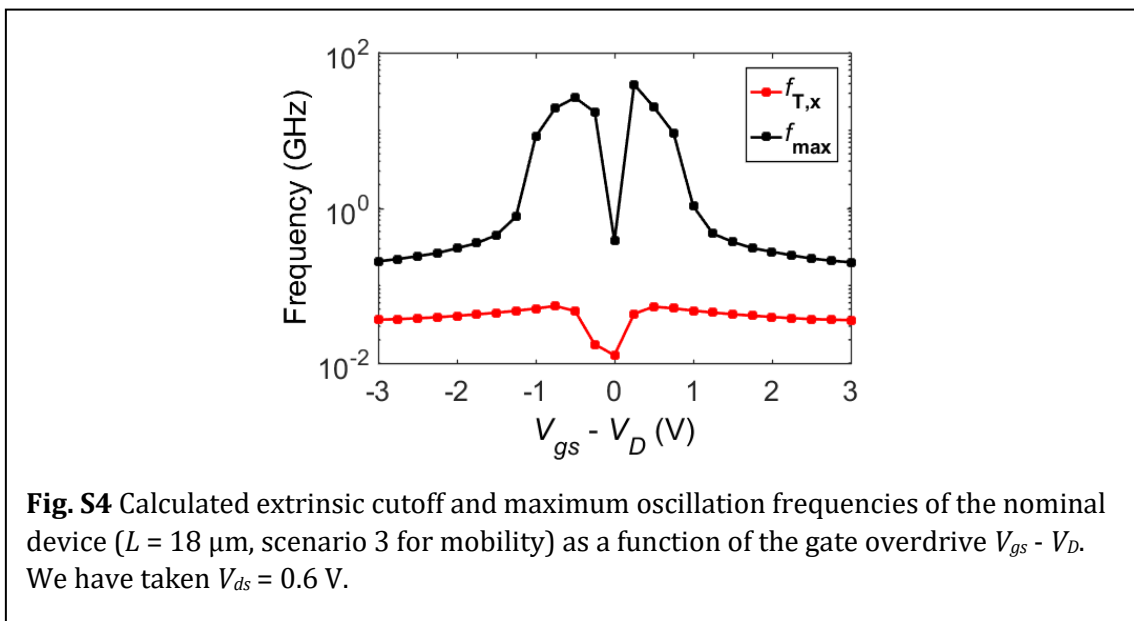
Section 4. Influence of the puddles in RF performance

Fig. S3 shows the effect of the carrier inhomogeneities (puddles) in the RF FoMs for different channel lengths. From Fig. S3b, it can be observed that the density of puddles does not significantly affect $f_{T,x}$. However, f_{max} slightly decreases as the puddle concentration increases, especially for short channels. This is caused by an increase of the output conductance with the presence of puddles, which is more noticeable in short-channel devices.



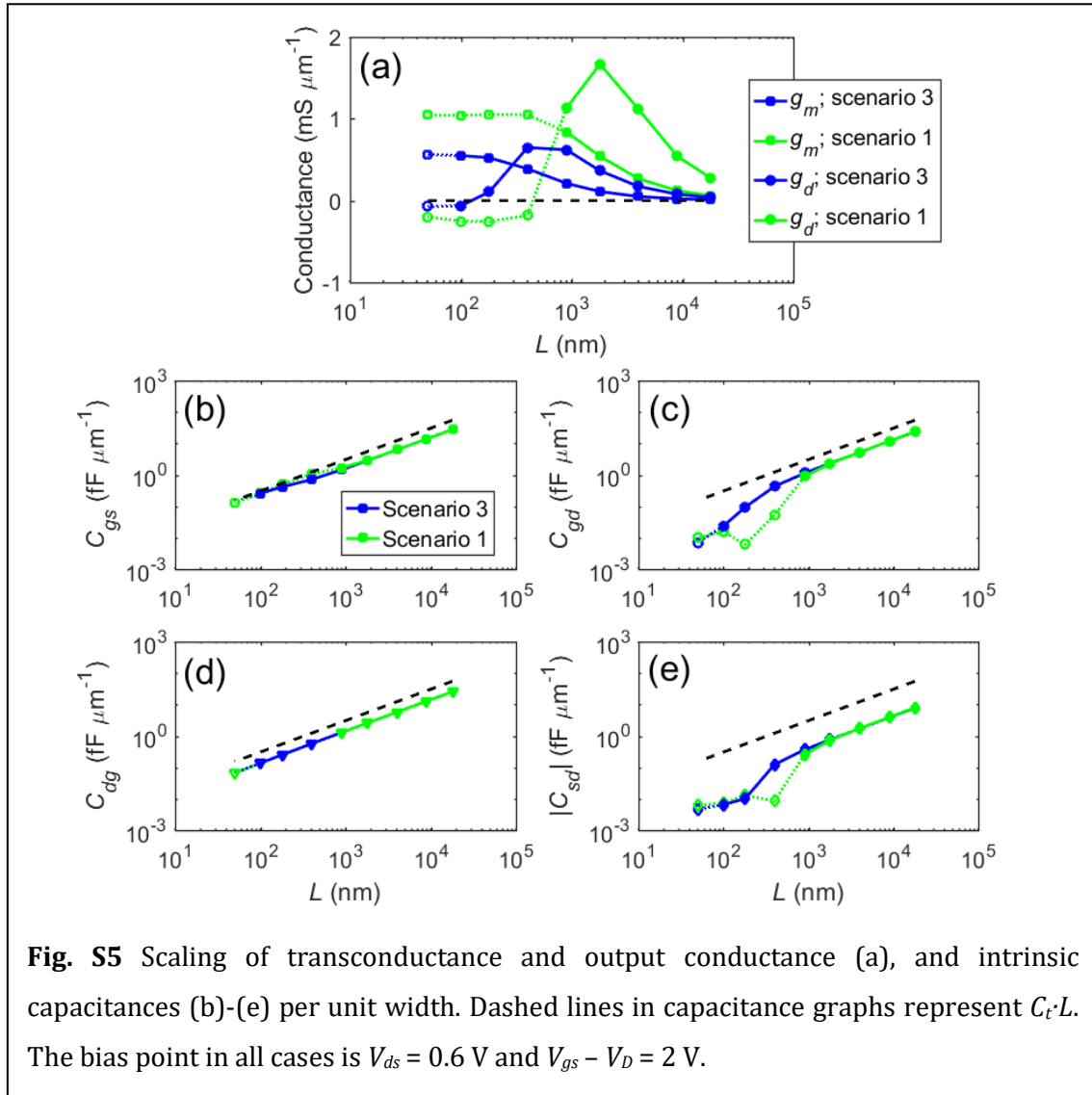
Section 5. Choice of the bias point for RF performance investigation

The GFET RF performances are, in general, dependent on the bias point. This can be seen in Fig. S4, which shows an exemplary plot of f_{max} and $f_{T,x}$ at $V_{ds} = 0.6$ V as a function of the gate voltage overdrive, $V_{gs} - V_D$, where V_D is the Dirac voltage. The graph exhibits two maxima and a minimum at $V_{gs} = V_D$, both maxima happening when the channel is pinched-off whether at the source and drain sides, respectively, and the minimum when the channel is pinched-off just at the channel center. For our RF investigation, we have chosen the combination $V_{ds} = 0.6$ V and $V_{gs} - V_D = 2$ V so the device is biased in the region where f_{max} and $f_{T,x}$ are quite insensitive to V_{gs} . This makes the comparison of different devices easier.



Section 6. Scaling of small-signal parameters

To fully understand the scaling of f_{max} and $f_{T,x}$, it is convenient to plot the behavior of the small-signal parameters of the GFET as a function of the channel length. Fig. S5 shows how they scale for the high and low mobility scenarios. The transconductance scales as $1/L$ at long channels but it reaches a maximum value for $L < 1 \mu\text{m}$, which is the reason for the observed saturation in the scaling of both f_{max} and $f_{T,x}$. Regarding g_d , it can even reach negative values in short-channel devices (negative differential resistance). Its large drop causes f_{max} to increase strongly, although its negative values may be the origin of the RF instability.² The intrinsic capacitances are approximately proportional to L although the magnitudes of C_{gd} and C_{sd} strongly decrease at small L , especially in the case of high mobility.



Section 7. Current-voltage characteristics

Fig. S6a compares the I-V characteristics of the 1.8 μm GFET with the experimental matched mobility, and a hypothetical GFET identical in geometry, but with the graphene channel just free from impurities and defects. The improvement in carrier mobility and saturation velocity increases I_{ds} in a factor ~ 3.5 . The transconductance g_m of the GFET also grows while some current saturation is observed. These features indicate that the RF performance improves accordingly as we move towards the ideal scenario where graphene is free of defects and impurities (see Fig. 6b,d). On the other hand, Fig. S6b shows that scaling the channel length down to 180 nm produces an improvement in g_m and a large increase of I_{ds} . Due to the increase of the electric field inside the channel, the drain current becomes limited by velocity saturation and the device saturates at a lower V_{ds} (~ 0.5 V).

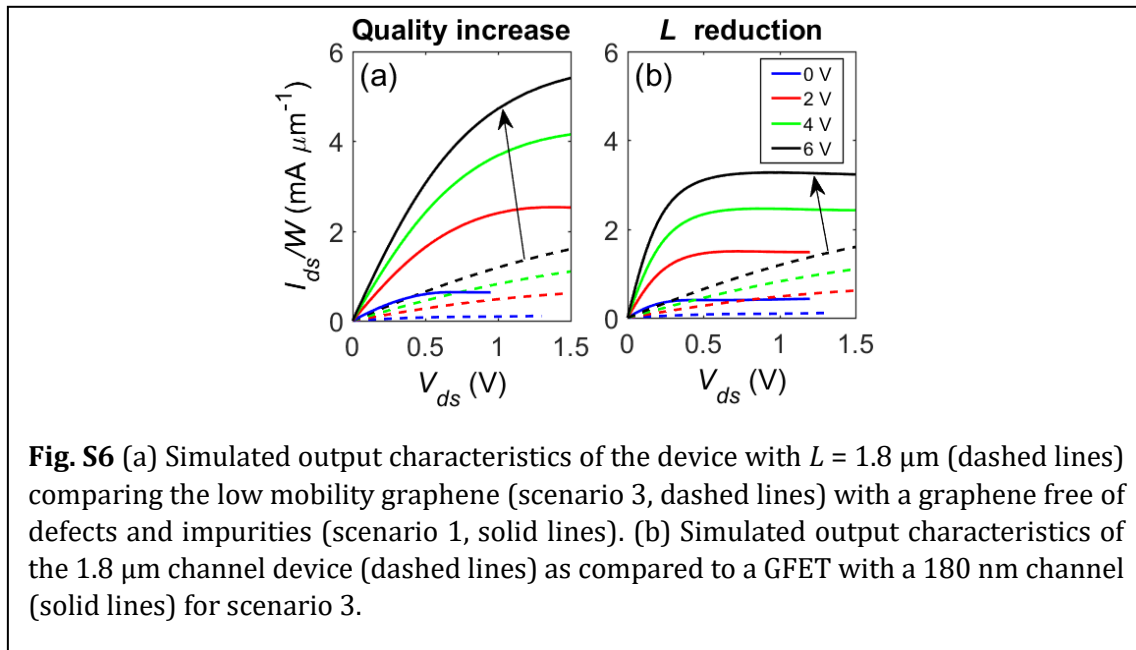


Fig. S6 (a) Simulated output characteristics of the device with $L = 1.8 \mu\text{m}$ (dashed lines) comparing the low mobility graphene (scenario 3, dashed lines) with a graphene free of defects and impurities (scenario 1, solid lines). (b) Simulated output characteristics of the 1.8 μm channel device (dashed lines) as compared to a GFET with a 180 nm channel (solid lines) for scenario 3.

References

- 1 Z. Chen and J. Appenzeller, in *IEEE International Electron Devices Meeting*, 2008, pp. 1–4.
- 2 R. Grassi, A. Gnudi, V. Di Lecce, E. Gnani, S. Reggiani and G. Baccarani, *IEEE Trans. Electron Devices*, 2014, **61**, 617–624.